Energy Storage Materials 20 (2019) 380–387

Contents lists available at ScienceDirect

Energy Storage Materials

journal homepage: www.elsevier.com/locate/ensm

Structural design of Ge-based anodes with chemical bonding for high-performance Na-ion batteries

Wenwu Li [a,b], Xinwei Li [c,**], Jun Liao [a], Bote Zhao [b], Lei Zhang [b], Yuchen Liu [b], Liang Huang [d,***], Yunyong Li [a], Meilin Liu [b,*]

[a] School of Materials and Energy, Guangdong University of Technology, Guangzhou, 510006, PR China
[b] School of Materials Science & Engineering, Georgia Institute of Technology, Atlanta, GA, 30332, USA
[c] Department of Mechanical and Energy Engineering, Southern University of Science and Technology, Shenzhen, 518071, PR China
[d] The State Key Laboratory of Refractories and Metallurgy, Wuhan University of Science and Technology (WUST), Wuhan, 430081, PR China

ARTICLE INFO

Keywords:
Ge-based
Chemical bonding
High-performance
Anode
Na-ion batteries

ABSTRACT

Ge-based anodes for Na-ion batteries (NIB) usually suffer from sluggish reaction kinetics, low initial Coulombic efficiency, poor reversible capacity, and short cycling life due mainly to its rigid diamond-like structure. Here we report our findings in characterization and application of a GeP anode with a flexible layered structure, synthesized by a simple mechanochemical method. When tested as the anode for NIBs, the GeP undergoes a self-healing Na-storage process that involves intercalation, conversion, and alloying, as co-revealed by *ex-situ* X-ray diffraction, HRTEM, Raman spectroscopy, and X-ray photoelectron spectroscopy analysis. The peculiar self-healing phenomenon derives from its ultra-low formation energy (−0.19 eV) for reconstruction of the original layered structure, as confirmed by first-principle calculations. The low formation energy also enables the formation of chemical bonding between layered GeP and graphite, thus achieving unprecedented performances among all reported anode materials based on Group IVA- and Group VA elements. The structural design strategy guided by formation energy of desirable phases is also applicable to the development of other energy-storage materials.

1. Introduction

Na-ion batteries (NIBs) has received increasing attention as an alternative power source to Li-ion batteries, as Na sources does not have the geopolitical issues that Li sources might have [1–5]. Si and Ge have been investigated as anodes for Na-ion batteries (NIBs) on the basis of the alloying mechanism in the form of Na_xM ($x < 1$, M = Si, Ge) [6–9]. However, these anodes with alloying mechanism for sodium storage usually suffer from sluggish reaction kinetics resulting from close-packed crystal lattice. Therefore, a variety of methods have been explored to address the problem. Na-inert metals like Fe, Co, etc. have been introduced into the electrode based on their potential buffer effect as an inactive matrix and enhanced e^- transfer capability during the deep discharge [10,11]. Nonetheless, these introduced Na-inert metals severely reduce energy density due largely to its heavy ineffective components for Na-storage. Afterwards, the Na-reactive O/S/Se have been introduced with the hope of greater reversible capacity [12,13]. Unfortunately, these Ge-based chalcogenide compounds were demonstrated to be unsuitable for anodes in NIBs due largely to their high working potentials above 1.0 V. In addition, the large polarization loss and poor initial Coulombic efficiencies are also almost unresolved because of their intrinsic large formation energy for Na_2O/S/Se etc..

Black P, due to its weaker electronegativity than oxygen, have been used as anode material for Na-ion batteries benefiting from large interlayer spacing and fast e^-/Na^+ transport capability [14–17]. However, the use of black P as anode material is still challenging because of its poor heat-management that causes spontaneous degradation into red P above 125 °C. To increase the safety and specific capacity, more attention has been paid to binary sodium-reactive Ge/Sn-P series [18,19]. Li et al discovered that a high-P content (70 wt.%, GeP_5) anode with a black P-like structure, which exhibits similar Na-storage behavior on the basis of traditional conversion reaction [18]. However, the structural

* Corresponding author.
** Corresponding author.
*** Corresponding author.
E-mail addresses: lixw@sustc.edu.cn (X. Li), huangliang1986@wust.edu.cn (L. Huang), meilin.liu@mse.gatech.edu (M. Liu).

https://doi.org/10.1016/j.ensm.2019.04.034
Received 22 February 2019; Received in revised form 14 April 2019; Accepted 24 April 2019
Available online 30 April 2019

similarity would incur the same issues as that of black P and the cycle-life is unsatisfactory because of the degradation in the crystal structure after the initial cycle. In addition, high P content (over 70 wt.%) in the composite may cause issues like degradation or spontaneous combustion due to a highly-reactive phosphide surface to oxygen and electrolyte. Recently, Park and Wang et al. discovered that layered Ge/SnP_3 undergoes an interesting self-healing Na-storage mechanism, thus achieving high Na-storage performances [19–22]. However, the fundamental insights into the structure-property relationship is still unclear. Therefore, it is important to design a self-healing structure with appropriate P content to achieve long cyclability and uncover the primary structure-performance relationship, which are of vital value to scientific understanding and practical application.

Here, we introduce 30 wt.% cheap P into Ge to form a layered GeP structure to produce a synergistic effect. When functioned as an anode for NIBs, the resulting GeP experiences a self-healing three stage Na-storage mechanism of intercalation, conversion, and alloying unveiled by XRD, Raman and XPS. The self-healing mechanism is attributed to its ultra-low formation energy of −0.19 eV, which allows the re-construction of the original layered structure on the basis of first-principles calculations. When mixed with graphite, the low formation energy also enables the strong interaction (P–C bonds) between layered GeP and graphite. Thus, the composite achieves faster Na-ion and electron transportation and unprecedented performance among all reported Group IVA- and Group VA-based anode materials.

2. Experimental section

2.1. Synthetic procedures

The pure GeP powder was prepared via a scalable high-energy mechanical ball milling method along with subsequent annealing at 380 °C. Typically, the Ge and red P powders in a given molar ratio 1:1 were poured into the steel vessel filled with argon and milled in the speed of 300 rpm for 3 h (Fritsch, Pulverisette-6). The as-milled GeP powder was then annealed at 380 °C for 0.5 h under argon atmosphere (heating rate of 2 °C min^{-1}). The GeP/C composite was hybridized by a second milling of the as-prepared GeP with commercially available graphite.

2.2. Materials characterization

The as-synthesized GeP powder was characterized by X-ray diffraction (XRD, Bruker D8 ADVANCE) using CuKα radiation. The morphology and microstructure were measured by the field-emission scanning electron microscope (FESEM, Hitach SU8220) and field-emission transmission electron microscope (FEI, Thermo Talos F200S TEM), respectively. The related samples were characterized by X-ray photoelectron spectroscopy (XPS, Thermo Fisher Escalab 250Xi using Al Kα radiation). Raman spectroscopy was tested by the Confocal Raman spectrometer (Raman, WTEC ALPHA300 with a 532 nm excitation laser).

2.3. Electrochemical measurement

The as-prepared GeP powder was blended into a slurry with conductive agent (carbon black) and binder (Li-PAA) in a mass ratio 7: 2: 1. The as-blended slurry was pasted onto a copper foil and dried for overnight (12 h) in a vacuum chamber (80 °C). The GeP/C composite (GeP: graphite = 7: 2, mass ratio) was directly mixed with LiPAA with a mass ratio of 9: 1. The typical loading was 1.2–1.5 mg cm^{-2}. The punched electrode species were assembled into a typical CR2032 coin-type cells in a glove box (Mbraun, Labmaster 130) filled with Ar atmosphere (H_2O, $O_2 < 0.05$ ppm). 1.0 M $NaCF_3SO_3$ dissolved in diglyme is utilized as electrolyte. Electrochemical Na-storage measurements were conducted on an automatic battery testing system named Hokuto Denko (HJ1001SD8) and Land (Wuhan).

2.4. Calculations detail

All DFT calculations were performed with the generalized gradient approximation (GGA) and Perdew-Burke-Ernzerhof (PBE) exchange correlation function as implemented in CASTEP. The ultrasoft pseudopotential was used to describe the electron-ion interaction. The plane-wave basis was utilized to represent the valence orbitals. The convergence of force, self-consistent field, displacement, energy were 3.0×10^{-2} eV $Å^{-1}$, 1.0×10^{-6} eV atom^{-1}, 1.0×10^{-3} Å, and 1.0×10^{-5} eV atom^{-1}, respectively. The Brillouin zone integration was sampled within a $1 \times 4 \times 1$ Monkhorst-Pack k-point mesh. A grid spacing of $\times 10^{-2}$ A^{-1} was utilized for the density of states (DOS) calculations on the basis of Monkhorst-Pack special k-point scheme. The complete LST/QST method was utilized to search transition states, starting with a linear synchronous transit optimization. The transition states approximation gained above was further utilized to carry out a quadratic synchronous transit maximization, and then by a conjugate gradient minimization. The saddle point can be found via the repeated search cycle. A value of 5×10^{-2} eV $Å^{-1}$ was utilized for all the root-mean-square forces on an atom in all calculations of transition states.

The formation energy E_f could be calculated on the basis of the following equation:

$$E_f = E_{MP} - \mu_M - \mu_X$$

where E_{MP} is the overall ground state energy of MP, μ_M is the related energy per atom in the stable elementary substance of Ge (space group FD-3M), Fe (space group IM-3M), Si (space group FD-3M) or Co (space group P63/MMC) atom. The μ_X is the energy per atom in P (space group Cmca CMCA) atom.

3. Results and discussion

Among various Group IVA-VA compounds, there exists a special layered structure in the GeP formula in the monoclinic phase with its formation energy as small as −0.19 eV based on our calculation. Generally, the formation energy can be utilized to evaluate the difficulty of formation or decomposition [23]. The small formation energy means that as an anode for NIBs, its initial crystal structure is potentially healed at high charge potentials, which would favor its high performances. Nevertheless, till now, to our best of knowledge, there is no report about the unique structure utilized for Na-storage, let alone, the structure-performance relationship behind. We synthesized GeP by ball milling of Ge and red phosphorus along with low-temperature heat treatment, avoiding the severe high-temperature and pressure synthesis condition in the 1970s [24]. It is noted that the annealing is a vital step for the successful synthesis of the layered GeP, as confirmed by the XRD pattern of the GeP precursor before annealing (Fig. S1). The crystal structure (Fig. 1a) shows a layered framework with a layered tunnel distance of ~6.3 Å. The open crystal lattice would guarantee the entrance of Na-ions and they would react with phosphorus atoms first and then germanium atoms to achieve large quantities of Na-ion storage. The XRD pattern (Fig. 1b) proves its monoclinic crystalline phase. The GeP aggregates with sizes up to several micrometers with irregular morphology (Fig. S2a and Fig. S2b). As shown in the SAED pattern (the inset of Fig. S3a), the well-defined rings with well-distributed spots accord well with that of the XRD fingerprint peaks. The HRTEM image (Fig. S3b) indicates that the main exposed crystal planes are (−311), (310), (−111), and (400) based on the measured d-spacings of 0.324 nm, 0.293 nm, 0.334 nm and 0.371 nm, respectively.

In light of the compositional and structural merits, specifically, two-fold Na-reactive constituents based on Na_xGe ($x < 1$) and Na_xP ($x < 3$), and layered crystal structure with ultralow formation energy endowed by little difference in the electronegativity between Ge and P, we anticipated the as-synthesized GeP would be highly reactive with Na to deliver great Na-storage performances with unique features. To demonstrate Na-

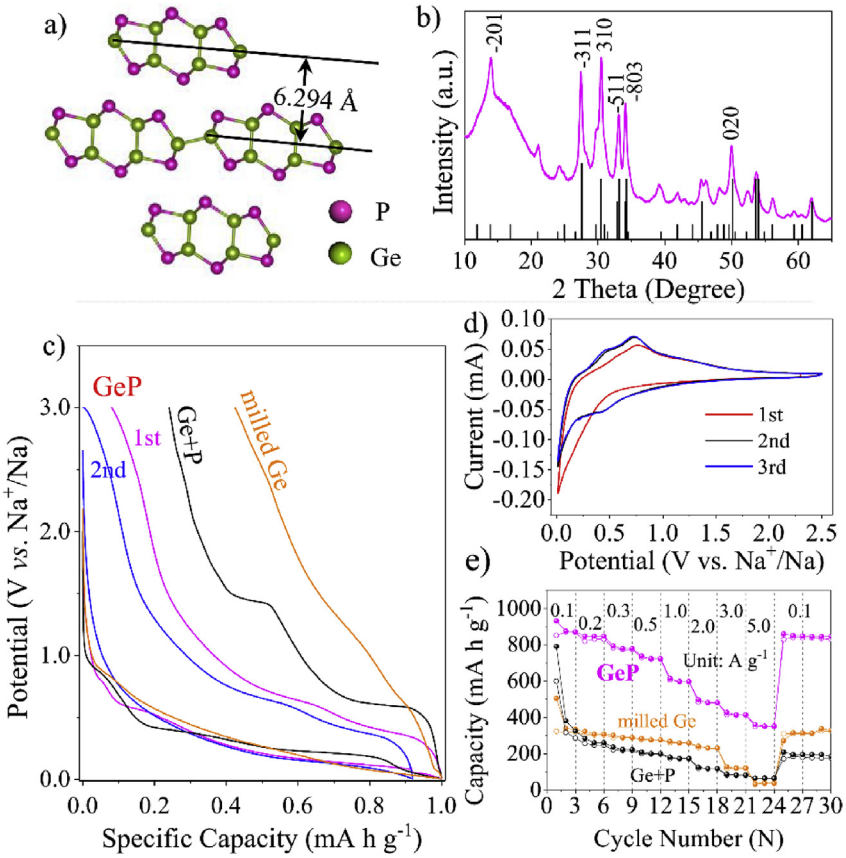

Fig. 1. a) the crystal structure of germanium monophosphide; b) the X-ray diffraction (XRD) pattern of the as-synthesized germanium monophosphide; c) the initial two discharge/charge profiles at 50 mA g^{-1} within the potential range of 0.005–3.0 V and their comparison with the first-cycle discharge/charge profiles of the milled Ge and the mixture of milled Ge and P (molar ratio of 1:1) electrodes; d) the initial three cyclic voltammetry curves at a scan rage of 0.05 mV s^{-1} within the potential range of 0.005–2.5 V; e) the rate performance comparison of the as-synthesized GeP, with the milled Ge and the mixture of milled Ge and P electrodes.

storage advantages of GeP, we compared the discharge/charge profiles (Fig. 1c) of as-synthesized GeP with the milled Ge and Ge+P mixture anodes. The GeP electrode delivers the smallest potential polarization loss and highest initial Coulombic efficiency. The GeP delivers an initial discharge/charge capacity of 900/840 mA h g^{-1}, thus leading to an initial Coulombic efficiency up to 93%. The Na-storage features shown by the discharge/charge profiles are well-consistent with CVs depicted by Fig. 1d. There is only one relatively sharp peak centered at ~0.25 V during the initial-cycle reduction, which can be assigned to the Na-ion uptake of the electrode. Reversely, there is one broad shoulder that can be split into three anodic peaks of 0.55 V, 0.75 V and 1.25 V, that can be assigned to the de-sodiation reaction of NaGe, Na_3P and Na_xGeP, respectively. From the second CV cycle onward, apart from the reduced polarization due to the initial-cycle activation processes, the CV curves are well-overlapped. This indicates that GeP has a highly reversible Na-storage capability [23]. All the CV results can be well-accorded with the initial two discharge/charge profiles as shown in Fig. 1c. From Fig. S4, we can see that the as-synthesized GeP anode can run over 40 cycles without obvious decay, which possesses a longer cycle stability than the mixture anode counterpart. Also seen from Fig. 1e, even at an aggressive current density of 5 A g^{-1}, the as-synthesized GeP can still deliver a reversible capacity of 360 mA h g^{-1}. This accounts for 40% of the initial reversible capacity at a current density of 100 mA g^{-1}, which is much better than the single-component milled Ge (41 mA h g^{-1}, 13%) and the mixture (63 mA h g^{-1}, 10%) electrode counterparts.

To explore the Na-storage mechanism of GeP, ex-situ XRD, HRTEM, Raman and XPS were carried out at the selected potential points as indicated in the discharge/charge profiles (Fig. 2a) operated at a current density rate of 50 mA g^{-1} within the potential window of 0.005–3.0 V. The corresponding XRD patterns collected at different states are shown in Fig. 2b. Stage I (from OCV to 0.38 V): the potential decrease corresponds well with the shifts of XRD fingerprint peak positions of (−311), (310), (−511), and (−803) towards the lower 2 theta angles. These relative shifts can be assigned to the large lattice expansion of the pristine GeP after the intercalation of Na-ion into the GeP interlayers along the direction of [010] to form Na_xGeP. Stage II: with increasing intercalated Na-ions, the intermediate Na_xGeP began to disintegrate into the mixture of Na_xP ($x < 3$) and Ge that can be proved by the fingerprint peak appearance of Ge in the XRD pattern at the potential of 0.18 V. Stage III: when the anode was fully discharged to 0.005 V, the electrode became amorphous as shown in the XRD due to the further Na-storage in the form of Na_xGe ($x = 1$). Stage IV: reversely, when charged back to 0.55 V, the fingerprint peaks of Ge appeared due to the removal of Na-ions from Na_xGe. Stage V: when charged back to 0.80 V, the weak fingerprint peaks of Na_xGeP appeared, therefore suggesting that the Na-ions can be further extracted from Na_3P to form Na_xGeP as an intermediate. Stage VI: with enough Na-ions removed from the Na_xGeP intermediate, the fingerprint peaks of the as-synthesized GeP reappeared, which can indicate the reconstruction of the pristine GeP during charging. To confirm the structural reversibility during cycling, we performed HRTEM examination of the samples after cycling. As shown in Fig. S5, the well-defined d-spacing of 0.63 nm is observed, which is consistent with the interlayer spacing of [-201] planes. Besides the evidence from the crystallography, we further performed Raman spectra on the as-synthesized GeP anode accompanied with the sodiation/desodiation process of the electrode at a current density 50 mA g^{-1} within the potential range of 0.005–3.0 V. As shown in Fig. 2c, we can see all the Raman characteristic bands of the as-synthesized GeP shifted to a lower wavenumber and the corresponding intensity diminished with the increased discharge depth. These phenomenon in the Raman spectroscopy imply the local structural topotactic transition induced by the increasing Na-ion intercalation amount into GeP interlayers to form Na_xGeP. In the subsequent discharge stage, the appearance of the fingerprint Raman peaks of Ge (299 cm^{-1}) indicate the intermediate phase Na_xGeP began to disintegrate into Ge and Na_xP based on traditional conversion reaction. Na_xP ($x < 3$) is invisible in Raman spectroscopy due largely to its low content and well-distribution within

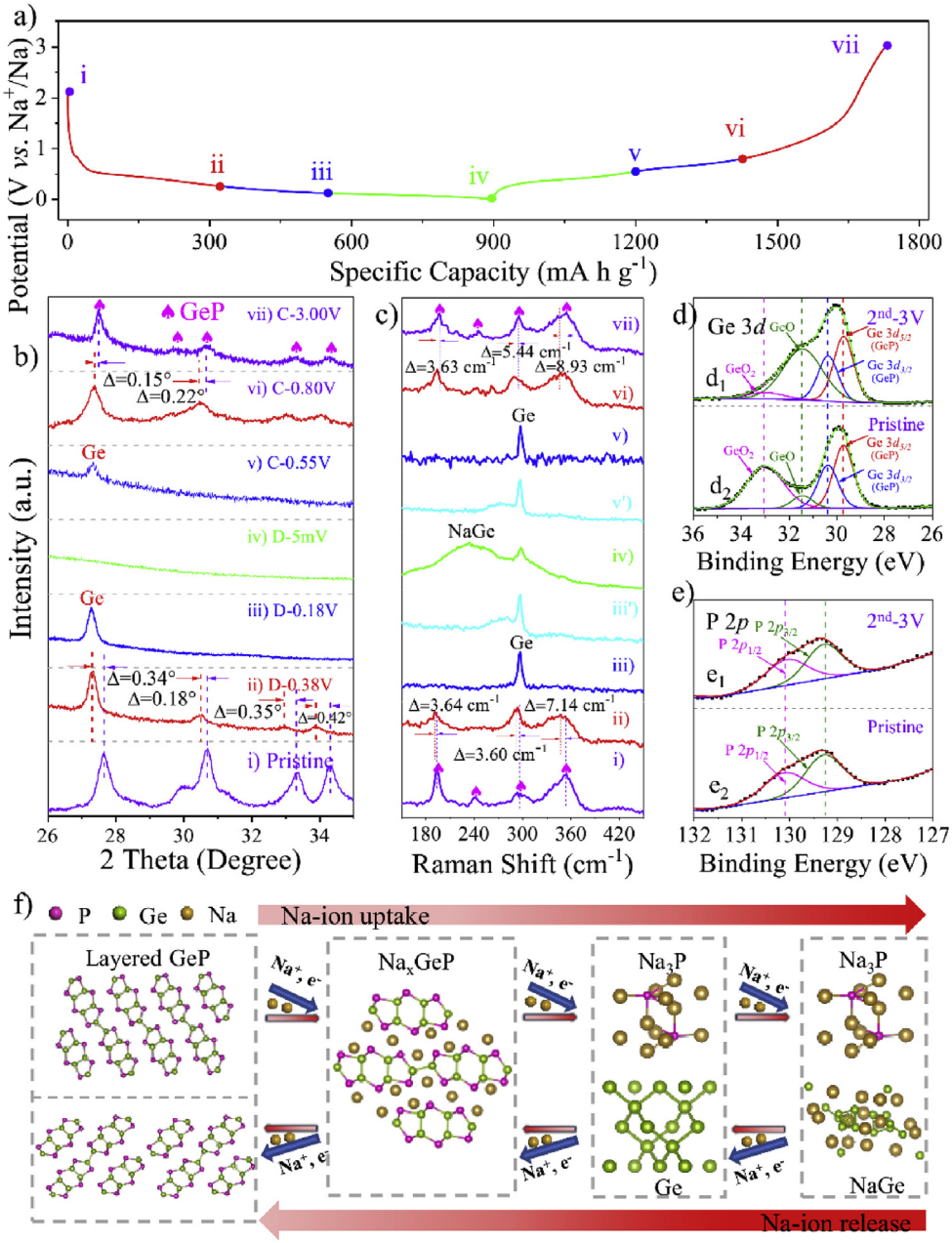

Fig. 2. a) the discharge/charge profiles marked for the ex-situ characterizations; b) the ex-situ XRD patterns at the given potential during the initial cycle; c) the ex-situ Raman spectroscopy at the given potential during the initial cycle; d) the ex-situ Ge 3d high-resolution spectra comparison of the pristine GeP and the electrode after the second cycle; e) the ex-situ P 2p high-resolution spectra comparison of the pristine GeP and the electrode after the second cycle; f) the illustrated Na-storage process.

the matrix, its poor crystallinity, or its decomposition when exposed to the air. As discharge continues, the fingerprint peak of Ge began to shift and became weaker until it disappeared at the end of discharge. By contrast, the Na_xGe characteristic peaks became stronger as the result of further sodiation of the resulting Ge. More surprisingly, when charged, all the corresponding procedures are reversible till the reappearance of the characteristic Raman peaks of the pristine GeP, which suggests the local structure of the as-synthesized GeP has been reconstructed. Therefore, the Raman results accord well with the conclusion of the crystallography above. In addition, we further performed the XPS contrasts of the pristine GeP powder and the electrode counterparts after the initial two cycles. As shown by the high-resolution Ge 3d spectra (Fig. 2d) and P 2p spectra (Fig. 2e), the electrode after the cycling look almost the same as the pristine powder counterparts, indicating the initial structure of the as-synthesized GeP was reformed.

To recap, the Na-storage mechanism of the as-synthesized GeP can be described as a three-fold mechanism of intercalation, conversion, and alloying during the sodiation process. All the reversed de-alloying, de-conversion, and de-intercalation process appears to be rather reversible, until the reappearance of the initial crystalline structure, thus accomplishing the ultra-high initial Coulombic efficiency up to 93%. Specifically, the Na-storage mechanism of the as-synthesized GeP can be illustrated in Fig. 2f and characterized as follows:

during discharging,

intercalation reaction: $GeP + x\ Na^+ + x\ e^- \rightarrow Na_xGeP$ (i)

conversion reaction: $Na_xGeP \rightarrow Na_xP + Ge$ (ii)

alloying reaction: $Ge + y\ Na^+ + y\ e^- \rightarrow Na_yGe$ (iii)

during charging,

de-alloying reaction: $Na_yGe \rightarrow Ge + y\ Na^+ + y\ e^-$ (iv)

de-conversion reaction: $Na_3P + Ge \rightarrow Na_xGeP + (3\text{-}x)\ Na^+ + (3\text{-}x)\ e^-$ (v)

de-intercalation reaction: $Na_xGeP \rightarrow GeP + x\ Na^+ + x\ e^-$ (vi)

In total: $GeP + 4\ Na^+ + 4\ e^- = Na_3P + NaGe$ (vii)

From the analysis above, the Na-storage behaviors and mechanism of the as-synthesized GeP, we can infer that it is an appealing anode candidate while hindered by its limited cycles due to its large volume change during the sodiation/desodiation processes. The large volume variation caused the cracking of active material, as shown in Fig. S6. As known, the introduction of low-cost graphite as the buffer matrix is a general method to prolong the cyclability. Inspired by this, we further composited the as-synthesized GeP with commercial graphite to form the highly-encapsulated composite by ball milling [25]. The high-magnitude FESEM image (Fig. S7a) shows that the composite shows refined micro-morphology. The halo-like ring within the dot-distributed SAED pattern (inset of Fig. S7b) further indicates the reduced crystallization of GeP, implying its strong interaction with layered graphite. The elemental mappings (Fig. S7d-Fig. S7f) of GeP/C composite indicate that the three elements Ge, P and C were well-distributed, similar to the framework (Fig. S7c). As shown in C 1s spectroscopy (Fig. 3a), the peak at 283.5 eV in GeP/C (Fig. 3) can be assigned to the P–C bonds [25]. Furthermore, in the high-resolution XPS spectroscopy of P 2p (Fig. 3b), there are two extra peaks located at 130.4 eV and 131.28 eV in the GeP/C composite, which also results from the formation of P–C bonds [25]. In addition, the P–C bonds can be validated by the extra Raman signal at 600-700 cm^{-1} in GeP/C shown in Fig. S8 [25]. As shown in Fig. S9, compared with GeP, there exist three extra peaks centered at 669 cm^{-1}, 682 cm^{-1} and 860 cm^{-1}, corresponding to P–C bonds [26]. The strong interaction between layered GeP and graphite within the electrode strengthens the electrode integrity during cycling and rate performance by virtue of faster Na-ion and electron transport. The initial three discharge/charge profiles of a GeP/C electrode are presented in Fig. S10. Compared with

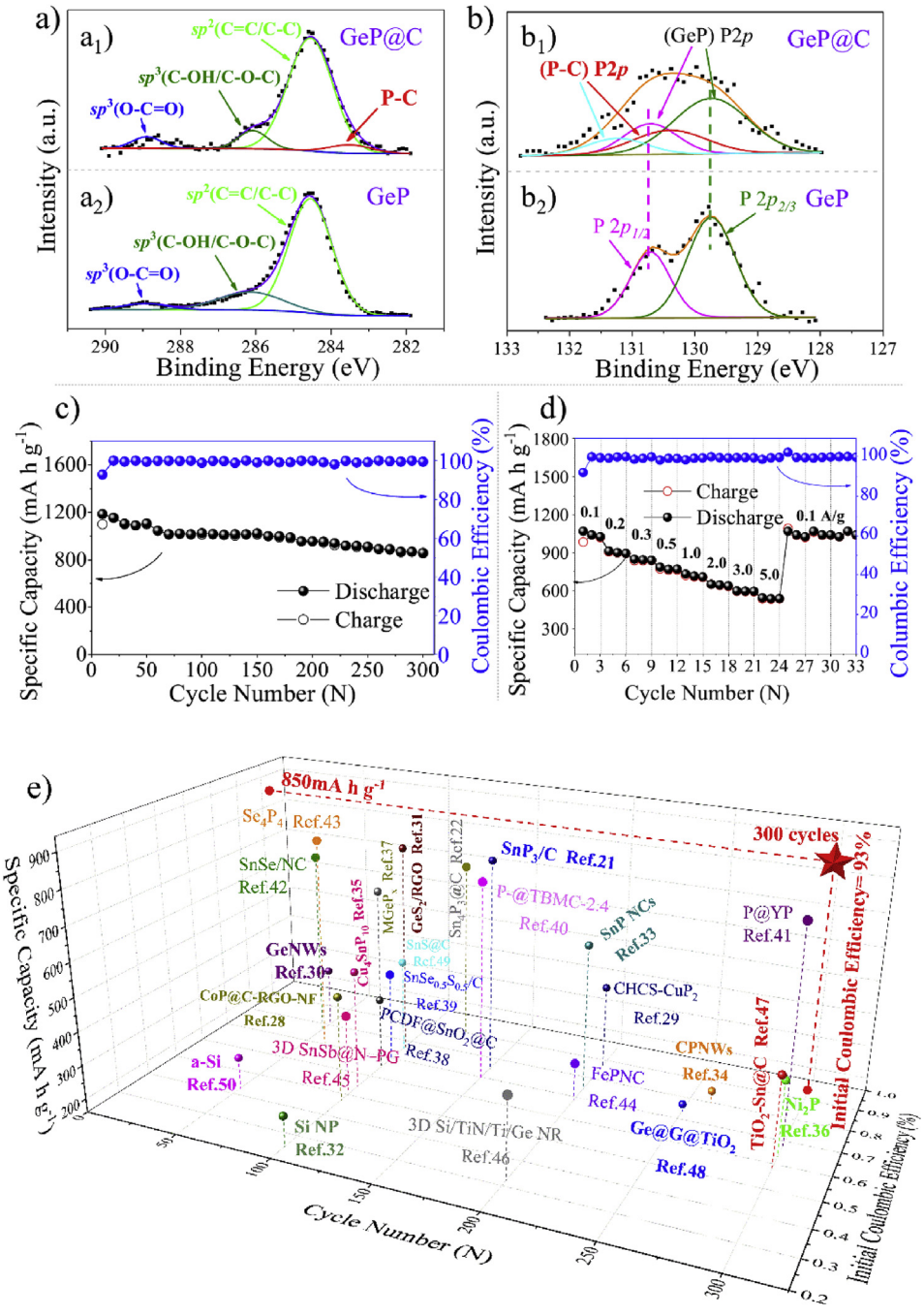

Fig. 3. P–C bond characterizations within the GeP/C nanocomposite: a) the high-resolution C 1s survey comparison of the as-synthesized GeP and GeP/C nanocomposite, respectively. b) the high-resolution P 2p survey comparison of the as-synthesized GeP and GeP/C nanocomposite, respectively. c, d) the cycle and rate performances of the as-synthesized GeP/C nanocomposite, e) the performance comparison of the as-synthesized GeP with other Group IVA- and Group VA-based anodes reported before in terms of initial Coulombic efficiency, remaining capacity after 300 cycles at relative small current density.

that of the pure GeP electrode, the GeP/C electrodes shows slightly reduced polarization due to enhanced electrical conductivity. Moreover, the slightly larger capacity is attributed to the contribution of ball-milled graphite and interfacial Na-storage [27]. The life-span (Fig. 3c) of the GeP/C electrode is extended to 300 cycles with a reversible capacity 850 mA h g^{-1} at 100 mA g^{-1}, which surpasses other reported Group IVA-based and Group VA-based anodes in terms of remaining capacity and initial Coulombic efficiency as compared in Fig. 3e [21,22,28–50]. The initial Coulombic efficiency of the GeP/C electrode is also above 90% and the second cycle is up to 99.5%, comparable to commercial graphite served for LIBs. The rate performance of GeP/C electrode was also evaluated and is shown in Fig. 3d, with promoting current density from 0.1 to 0.2, 0.3, 0.5, 1, 2, and 3 A g^{-1}, reversible capacities of 1020, 894, 840, 763, 704, 638, and 592 mA h g^{-1} was achieved. Even at a high current density of 5 A g^{-1}, the reversible capacity can still maintain up to 533 mA h g^{-1}. The high performances can be attributed to the following three features: 1) the self-healing Na-storage mechanism alleviates the electrode structure degradation, 2) the Na-intercalation compound Na_x-GeP achieves metallic conductivity, and 3) the formed chemical bonding (P–C bonds) between layered GeP and graphite not only helps maintain excellent electrical conduction and Na-ion diffusion, but also accommodates the volume variation during cycling.

To give more in-depth insights into inherent Na-ion diffusion properties and the effect of chemical bonding (P–C bonds) on Na-ion diffusion properties and electronic structure of the as-synthesized GeP, a new anode material without similar crystal structure reported for Na-storage before, we evaluate the Na-ion mobility together with the corresponding pathways and electronic structure within the two configurations: 1) pure GeP phase and 2) GeP/C composite with P–C bonding via the first-principles calculations at the atomic level [51,52]. Within the GeP structure, there are three possible diffusion paths, which are along the [010] direction (Fig. 4a), [102] direction (Fig. S11), and another diffusion direction perpendicular to the interlayer direction (Fig. S12). Compared with the energy barriers among the three directions above (Fig. 4c, Fig. S11b, and Fig. S12b), the lowest energy barrier is only 0.28 eV (Fig. 4d) along the [010] direction, which is much lower than the Ge counterpart (1.02 eV, Fig. 4c). From the density of state (DOS), as compared with the pristine GeP (Fig. 4f), the GeP with the intercalation of Na has metallic conductivity endowed by the co-introduction of electrons with the Na-ions since the density distribution at fermi level is not zero, as shown in Fig. 4g. Therefore, these simulation results rationalize the observed superiority in Na-storage behavior of the layered GeP, e.g. high rate capability and small polarization loss, compared with the ball milled Ge and the Ge+P mixture electrode counterparts. Furthermore, we calculated the effect of the chemical bonding on the Na-ion diffusion (P–C bonds, as shown in Fig. 4b). As compared in Fig. 4c–e, the Na-ion diffusion energy barrier can be further reduced to 0.10 eV (Fig. 4e) on the GeP/C composite with of P–C bonding. In addition, the redox sites can receive electrons transferred easily from hexagon carbon rings. Compared with the total DOS value (Fig. 4f) of the pristine GeP, the GeP/C composite (Fig. 4h) shows higher DOS near Fermi level, indicating a metallic electronic property due to the formation of P–C bonding. To validate the enhanced electronic conductivity, we performed the electrochemical impedance spectra (EIS) tests. As shown in Fig. S13, the charge transfer resistance, Rct, of the GeP/C electrode is significantly smaller than that of the GeP electrode, implying that the electrical conductivity of the composite electrode is enhanced [25]. Therefore, GeP/C nanocomposite demonstrates better electrochemical Na-storage performance.

To provide an in-depth insight into the mechanism behind the interesting healing ability of the crystal structure driven by the increasing potential during the de-sodiation process and the fundamental reasons for bonding between layered GeP and graphite, first-principles calculations were carried out to evaluate the difficulty of chemical bond cleavage or re-construction [23,53] based on formation energy. As listed in Table 1, GeP has the lowest formation energy (only −0.19 eV)

Table 1
The formation energy comparison of GeP, SiP, CoP, and FeP based on the first-principle calculation.

Mater.	GeP	SiP	CoP	FeP
Formation Energy/eV	−0.19	−0.42	−1.57	−1.9

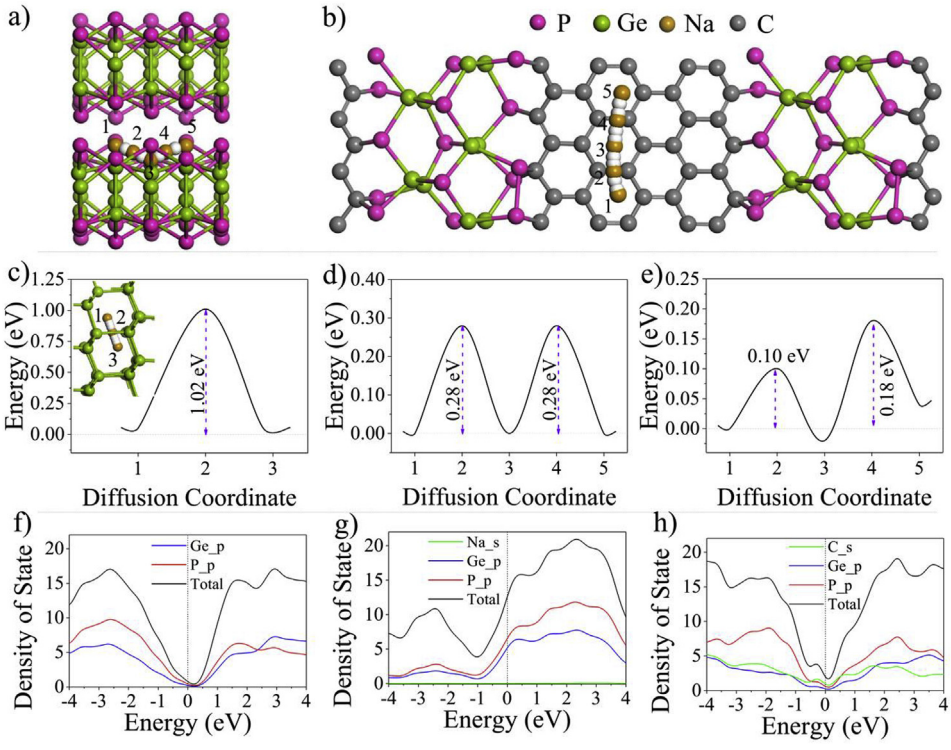

Fig. 4. a) The simulated model of the as-synthesized GeP used for Na-ion diffusion along the [010] direction; b) The simulated model of the chemical bonding (P–C bonds) between the layered GeP and layered graphite; c) the Na-ion diffusion energy barrier of Ge and the inset is the related diffusion path; d) the Na-ion diffusion energy barrier along the [010] direction corresponding to the diffusion path shown in a); e) the Na-ion diffusion energy barrier along the chemical bonding between the layered GeP and layered graphite corresponding to the diffusion path shown in b); f) the density of state (DOS) of the pristine GeP; g) the density of state (DOS) of the GeP with Na-ion intercalation within the interlayer; h) the density of state (DOS) of the GeP/C composite with chemical bonding between the layered GeP and layered graphite.

compared with other phosphides like SiP, CoP, and FeP. The small formation energy of GeP means that it is relatively easy to synthesize and decompose under mild experimental conditions. Therefore, the small driving force like electrochemically charging is sufficient enough to overcome the energy barrier to re-construct its original bonding chemistry. On the other hand, upon the destruction of the crystal structure and the bonding, the layered GeP was easy to bind with graphite to form P–C bonds, which would improve Na-ion and electronic transportation.

4. Conclusion

In summary, by introducing a small fraction of P into Ge, we transformed the diamond structure into a layered structure with ultralow formation energy via a facile two-step method of ball milling followed by sintering. When functioned as an anode for NIBs, the layered GeP delivered much better Na-storage performance than its corresponding Ge and Ge+P mixture anodes. The superiority is due to its low activation energy of 0.28 eV along the [010] diffusion direction, which is lower than that of Ge (1.02 eV) based on first-principles calculations. Furthermore, the Na_xGeP intermediate product has metallic conductivity caused by the intercalation of Na-ion. The ex-situ XRD, HRTEM, Raman and XPS techniques demonstrated that GeP experiences a self-healing three-step Na-storage mechanism: intercalation, conversion and alloying reaction. The self-healing capability to re-construct its layered crystal structure is due to its low formation energy based on first-principles calculations. When composited with graphite, the low formation energy also assists to form strong interactions (P–C bonds) between layered GeP and graphite. These bonds help further enhance the Na^+ and e^- transfer based on our simulated calculation, thus accomplishing the best performances among all the reported Group IVA-based and Group VA-based anodes for SIBs. The synthesis strategy with atomically designing a material with low formation energy can be extended to other anode materials for metal ion batteries.

Notes

The authors declare no competing financial interest.

Acknowledgment

We acknowledge the National Natural Science Foundation of China (21701030, 51801096, 51702241), Guangdong Province Natural Science Foundation(2017A030310241), Innovative talents cultivation project of outstanding youth in Guangdong Province (2016KQNCX038), Science and Technology Planning Project of Guangzhou City (201804010392), China Postdoctoral Science Foundation funded project (No. 1112000139), Guangdong Natural Science Foundation for Distinguished Young Scholar (2016A030306030) Guangdong Innovative and Entrepreneurial Research Team Program (No. 2014ZT05N200), and US National Science Foundation (DMR-1742828). The authors acknowledge the use of facilities in Guangdong University of Technology, Georgia Institute of Technology, and Southern University of Science and Technology.

Appendix A. Supplementary data

Supplementary data to this article can be found online at https://doi.org/10.1016/j.ensm.2019.04.034.

References

[1] C. Liu, X. Han, Y. cao, S. Zhang, Y. Zhang, J. Sun, Topological construction of phosphorus and carbon composite and its application in energy storage, Energy Storage Mater. (2018). https://doi.org/10.1016/j.ensm.2018.10.021.
[2] W. Liu, H. Zhi, X. Yu, Recent progress in phosphorus based anode materials for lithium/sodium ion batteries, Energy Storage Mater. 16 (2019) 290–322.
[3] X. Sun, W. Li, X. Zhong, Y. Yu, Superior sodium storage in phosphorus@porous multichannel flexible freestanding carbon nanofibers, Energy Storage Mater. 9 (2017) 112–118.
[4] Y. Liu, N. Zhang, X. Liu, C. Chen, L. Fan, L. Jiao, Red phosphorus nanoparticles embedded in porous N-doped carbon nanofibers as high-performance anode for sodium-ion batteries, Energy Storage Mater. 9 (2017) 170–178.
[5] J. Sun, H.-W. Lee, M. Pasta, Y. Sun, W. Liu, Y. Li, H.R. Lee, N. Liu, Y. Cui, Carbothermic reduction synthesis of red phosphorus-filled 3D carbon material as a high-capacity anode for sodium ion batteries, Energy Storage Mater. 4 (2016) 130–136.
[6] S. Huang, L. Liu, Y. Zheng, Y. Wang, D. Kong, Y. Zhang, Y. Shi, L. Zhang, O.G. Schmidt, H.Y. Yang, Efficient sodium storage in rolled-up amorphous Si nanomembranes, Adv. Mater. 30 (2018) 1706637.
[7] Y. Xu, E. Swaans, S. Basak, H.W. Zandbergen, D.M. Borsa, F.M. Mulder, Reversible Na-ion uptake in Si nanoparticles, Adv. Energy Mater. 6 (2016) 1501436.
[8] A. Kohandehghan, K. Cui, M. Kupsta, J. Ding, M. Lotfabad, W.P. Kalisvaart, D. Mitlin, Activation with Li enables facile sodium storage in germanium, Nano Lett. 14 (2014) 5873–5882.
[9] X. Lu, E.R. Adkins, Y. He, L. Zhong, L. Luo, S.X. Mao, C.-M. Wang, B.A. Korgel, Germanium as a sodium ion battery material: in situ TEM reveals fast sodiation kinetics with high capacity, Chem. Mater. 28 (2016) 1236–1242.
[10] J. Liu, Y. Wen, P.A. Aken, J. Maier, Y. Yu, Facile synthesis of highly porous Ni–Sn intermetallic microcages with excellent electrochemical performance for lithium and sodium storage, Nano Lett. 14 (2014) 6387–6392.
[11] Y. Yui, Y. Ono, M. Hayashi, Y. Nemoto, K. Hayashi, K. Asakura, H. Kitabayashi, Sodium-ion insertion/extraction properties of Sn-Co anodes and Na pre-doped Sn-Co anodes, J. Electrochem. Soc. 162 (2015) A3098–A3102.
[12] J.-H. Kim, J.H. Yun, D.K. Kim, A robust approach for efficient sodium storage of GeS_2 hybrid anode by electrochemically driven amorphization, Adv. Energy Mater. 8 (2018) 1703499.
[13] A.-R. Park, C.-M. Park, Cubic crystal-structured SnTe for superior Li- and Na-ion battery anodes, ACS Nano 11 (2017) 6074–6084.
[14] S. Liu, H. Xu, X. Bian, J. Feng, J. Liu, Y. Yang, C. Yuan, Y. An, R. Fan, L. Ci, Nanoporous red phosphorus on reduced graphene oxide as superior anode for sodium-ion batteries, ACS Nano 12 (2018) 7380–7387.
[15] Y. Hu, B. Li, X. Jiao, C. Zhang, X. Dai, J. Song, Stable cycling of phosphorus anode for sodium-ion batteries through chemical bonding with sulfurized polyacrylonitrile, Adv. Funct. Mater. 28 (2018) 1801010.
[16] W. Li, S. Hu, X. Luo, Z. Li, X. Sun, M. Li, F. Liu, Y. Yu, Confined amorphous red phosphorus in MOF-derived N-doped microporous carbon as a superior anode for sodium-ion battery, Adv. Mater. 29 (2017) 1605820.
[17] T. Yuan, J. Ruan, C. Peng, H. Sun, Y. Pang, J. Yang, Z.-F. Ma, S. Zheng, 3D red phosphorus/sheared CNT sponge for high performance lithium-ion battery anodes, Energy Storage Mater. 13 (2018) 267–273.
[18] W. Li, H. Li, Z. Lu, L. Gan, L. Ke, T. Zhai, H. Zhou, Layered phosphorus-like GeP_5: a promising anode candidate with high initial Coulombic efficiency and large capacity for lithium ion batteries, Energy Environ. Sci. 8 (2015) 3629–3636.
[19] K.-H. Nam, K.-J. Jeon, C.-M. Park, Layered germanium phosphide-based anodes for high-performance lithium- and sodium-ion batteries, Energy Storage Mater. (2018). https://doi.org/10.1016/j.ensm.2018.07.026.
[20] Y. Xu, B. Peng, F.M. Mulder, A high-rate and ultrastable sodium ion anode based on a novel Sn_4P_3-P@graphene nanocomposite, Adv. Energy Mater. 8 (2018) 1701847.
[21] X. Fan, J. Mao, Y. Zhu, C. Luo, L. Suo, T. Gao, F. Han, S.-C. Liou, C. Wang, Superior stable self-healing SnP_3 anode for sodium-ion batteries, Adv. Energy Mater. 5 (2015) 1500174.
[22] X. Fan, T. Gao, C. Luo, F. Wang, J. Hu, C. Wang, Superior reversible tin phosphide-carbon spheres for sodium ion battery anode, Nano Energy 38 (2017) 350–357.
[23] Y. Wei, L. Huang, J. He, Y. Guo, R. Qin, H. Li, T. Zhai, Healable structure triggered by thermal/electrochemical force in layered $GeSe_2$ for high performance Li-ion batteries, Adv. Energy Mater. 8 (2018) 1703635.
[24] P.C. Donohue, H.S. Young, Synthesis, structure, and superconductivity of nnew high pressure phases in the systems Ge-P and Ge-As, J. Solid State Chem. 1 (1970) 143–149.
[25] J. Sun, G. Zheng, H.W. Lee, N. Liu, H. Wang, H. Yao, W. Yang, Y. Cui, Formation of stable phosphorus-carbon bond for enhanced performance in black phosphorus nanoparticle-graphite composite battery anodes, Nano Lett. 14 (2014) 4573–4580.
[26] M. Ihsan-Ul-Haq, H. Huang, J. Cui, S. Yao, J. Wu, W.G. Chong, B. Huang, J.K. Kim, Chemical interactions between red P and functional groups in NiP_3/CNT composite anodes for enhanced sodium storage, J. Mater. Chem. A 6 (2018) 20184–20194.
[27] B. Long, M.S. Balogun, L. Luo, W.T. Qiu, Y. Luo, S.Q. Song, Y.X. Tong, Phase boundary derived pseudocapacitance enhanced nickel-based composites for electrochemical energy storage devices, Adv. Energy Mater. 8 (2018) 1701681.
[28] X. Ge, Z. Li, L. Yin, Metal-organic frameworks derived porous core/shell CoP@C polyhedrons anchored on 3D reduced graphene oxide networks as anode for sodium-ion battery, Nano Energy 32 (2017) 117–124.
[29] S. Chen, F. Wu, L. Shen, Y. Huang, S.K. Sinha, V. Srot, P.A. van Aken, J. Maier, Y. Yu, Cross-linking hollow carbon sheet encapsulated CuP_2 nanocomposites for high energy density sodium-ion batteries, ACS Nano 12 (2018) 7018–7027.
[30] A. Kohandehghan, K. Cui, M. Kupsta, J. Ding, E.M. Lotfabad, W.P. Kalisvaart, D. Mitlin, Activation with Li enables facile sodium storage in germanium, Nano Lett. 14 (2014) 5873–5882.
[31] J.-H. Kim, J.H. Yun, D.K. Kim, A robust approach for efficient sodium storage of GeS_2 hybrid anode by electrochemically driven amorphization, Adv. Energy Mater. 8 (2018) 1703499.
[32] Y. Xu, E. Swaans, S. Basak, H.W. Zandbergen, D.M. Borsa, F.M. Mulder, Reversible Na-ion uptake in Si nanoparticles, Adv. Energy Mater. 6 (2016) 1501436.

[33] J. Liu, S. Wang, K. Kravchyk, M. Ibáñez, F. Krumeich, R. Widmer, D. Nasiou, M. Meyns, J. Llorca, J. Arbiol, M.V. Kovalenko, A. Cabot, SnP nanocrystals as anode material for Na-ion battery, J. Mater. Chem. A 6 (2018) 10958–10966.
[34] M. Fan, Y. Chen, Y. Xie, T. Yang, X. Shen, N. Xu, H. Yu, C. Yan, Half-cell and full-cell applications of highly stable and binder-free sodium ion batteries based on Cu_3P nanowire anodes, Adv. Funct. Mater. 26 (2016) 5019–5027.
[35] D. Lan, W. Wang, Q. Li, Cu_4SnP_{10} as a promising anode material for sodium ion batteries, Nano Energy 39 (2017) 506–512.
[36] C. Wu, P. Kopold, P.A. van Aken, J. Maier, Y. Yu, High performance graphene/Ni_2P hybrid anodes for lithium and sodium storage through 3D yolk-shell-like nanostructural design, Adv. Mater. 29 (2017) 1604015.
[37] K.-W. Tseng, S.-B. Huang, W.-C. Chang, H.-Y. Tuan, Synthesis of mesoporous germanium phosphide microspheres for high-performance lithium-ion and sodium-ion battery anodes, Chem. Mater. 30 (2018) 4440–4447.
[38] M. Dirican, Y. Lu, Y. Ge, O. Yildiz, X. Zhang, Carbon-confined SnO_2-electrodeposited porous carbon nanofiber composite as high-capacity sodium-ion battery anode material, ACS Appl. Mater. Interfaces 7 (2015) 18387–18396.
[39] Q. Tang, Y. Cui, J. Wu, D. Qu, A.P. Baker, Y. Ma, X. Song, Y. Liu, Ternary tin selenium sulfide ($SnSe_{0.5}S_{0.5}$) nano alloy as the high-performance anode for lithium-ion and sodium-ion batteries, Nano Energy 41 (2017) 377–386.
[40] D. Liu, X. Huang, D. Qu, D. Zheng, G. Wang, J. Harris, J. Si, T. Ding, J. Chen, D. Qu, Confined phosphorus in carbon nanotube-backboned mesoporous carbon as superior anode material for sodium/potassium-ion batteries, Nano Energy 52 (2018) 1–10.
[41] Yu, J. Song, D. Wang, D. Wang, Advanced anode for sodium-ion battery with promising long cycling stability achieved by tuning phosphorus-carbon nanostructures, Nano Energy 40 (2017) 550–558.
[42] X. Ren, J. Wang, D. Zhu, Q. Li, W. Tian, L. Wang, J. Zhang, L. Miao, P.K. Chu, K. Huo, Sn-C bonding riveted SnSe nanoplates vertically grown on nitrogen-doped carbon nanobelts for high-performance sodium-ion battery anodes, Nano Energy 54 (2018) 322–330.
[43] Y. Lu, P. Zhou, K. Lei, Q. Zhao, Z. Tao, J. Chen, Selenium phosphide (Se_4P_4) as a new and promising anode material for sodium-ion batteries, Adv. Energy Mater. 7 (2017) 1601973.
[44] Y. Von Lim, S. Huang, Y. Zhang, D. Kong, Y. Wang, L. Guo, J. Zhang, Y. Shi, T.P. Chen, L.K. Ang, H.Y. Yang, Bifunctional porous iron phosphide/carbon nanostructure enabled high-performance sodium-ion battery and hydrogen evolution reaction, Energy Storage Mater. 15 (2018) 98–107.
[45] J. Qin, T. Wang, D. Liu, E. Liu, N. Zhao, C. Shi, F. He, L. Ma, C. He, A top-down strategy toward SnSb in-plane nanoconfined 3D N-doped porous graphene composite microspheres for high performance Na-ion battery anode, Adv. Mater. 30 (2018) 1704670.
[46] C. Yue, Y. Yu, S. Sun, X. He, B. Chen, W. Lin, B. Xu, M. Zheng, S. Wu, J. Li, J. Kang, L. Lin, High performance 3D Si/Ge nanorods array anode buffered by TiN/Ti interlayer for sodium-ion batteries, Adv. Funct. Mater. 25 (2015) 1386–1392.
[47] M. Mao, F. Yan, C. Cui, J. Ma, M. Zhang, T. Wang, C. Wang, Pipe-wire TiO_2-Sn@carbon nanofibers paper anodes for lithium and sodium ion batteries, Nano Lett. 17 (2017) 3830–3836.
[48] X. Wang, L. Fan, D. Gong, J. Zhu, Q. Zhang, B. Lu, Core-Shell Ge@graphene@TiO_2 nanofibers as a high-capacity and cycle-stable Anode for lithium and sodium ion battery, Adv. Funct. Mater. 26 (2016) 1104–1111.
[49] P. He, Y. Fang, X.-Y. Yu, X.W.D. Lou, Hierarchical nanotubes constructed by carbon-coated ultrathin SnS nanosheets for fast capacitive sodium storage, Angew. Chem. Int. Ed. 56 (2017) 12202–12205.
[50] S. Huang, L. Liu, Y. Zheng, Y. Wang, D. Kong, Y. Zhang, Y. Shi, L. Zhang, O.G. Schmidt, H.Y. Yang, Efficient sodium storage in rolled-up amorphous Si nanomembranes, Adv. Mater. 30 (2018) 1706637.
[51] S. Shi, Z. Li, Y. Sun, B. Wang, Q. Liu, Y. Hou, S. Huang, J. Huang, Y. Zhao, A covalent heterostructure of monodisperse Ni_2P immobilized on N, P-co-doped carbon nanosheets for high performance sodium/lithium storage, Nano Energy 48 (2018) 510–517.
[52] D. Kim, K. Zhang, M. Cho, Y.-M. Kang, Critical design factors for kinetically favorable P-based compounds toward the alloying with Na ions for high-power sodium-ion batteries, Energy Environ. Sci. (2019). https://doi.org/10.1039/C9EE00283A.
[53] W. Li, X. Li, J. Yu, J. Liao, B. Zhao, L. Huang, A. Abdelhafiz, H. Zhang, J. Wang, Z. Guo, M. Liu, Nano Energy (2019), https://doi.org/10.1016/j.nanoen.2019.04.080.